Materials Advances

ROYAL SOCIETY OF CHEMISTRY

PAPER

View Article Online
View Journal | View Issue



Check for updates

Cite this: *Mater. Adv.*, 2025, **6**, 9505

# Correlating critical behaviour and the magnetocaloric effect in Fe–Hf–Zr–B–Cu metallic glasses

Anjana Vinod,[abc] D. Arvindha Babu,[d] Manivel Raja Muthuvel,[d] S. Srinath[e] and W. Madhuri *[f]

Received 18th August 2025,
Accepted 26th September 2025

DOI: 10.1039/d5ma00922g

rsc.li/materials-advances

This research is a systematic experimental investigation of the structural and magnetic properties of a series of $Fe_{88-x}Hf_xZr_7B_4Cu_1$ ($x$ = 2 & 4) metallic glass ribbons, with a particular emphasis on their magnetocaloric effect (MCE) and magnetic phase transition (MPT) behaviour. Utilizing the Kouvel–Fisher method, critical isotherm analysis, and modified Arrott plots, the critical exponents ($\beta$, $\gamma$, $\delta$) are estimated to be in close agreement with the 3D-Heisenberg model. Using the Maxwell thermodynamic relation, we determined the maximal isothermal entropy change ($-\Delta S_M$) for the $Fe_{88-x}Hf_xZr_7B_4Cu_1$ ($x$ = 2 & 4) ribbons. The $Fe_{86}Hf_2Zr_7B_4Cu_1$ ribbons display an RCP of approximately 61.23 J kg$^{-1}$ at a Curie transition temperature of 298 K, while the $Fe_{84}Hf_4Zr_7B_4Cu_1$ ribbons exhibit an RCP of 33.0 J kg$^{-1}$ at a Curie transition temperature of 312 K under a magnetic field of $\mu_0 H$ = 2.5 T. This paves the way for the development of innovative magnetic refrigerants that are specific to efficient active cooling technologies near room temperature.

## 1. Introduction

The concept of sustainable development is a paradigmatic that seeks to reconcile the needs of contemporary societies with the imperative of safeguarding the planet's resources for future generations.[1] This comprehensive strategy integrates economic, social, and environmental factors to emphasize long-term harmony and balance.[2] By taking a comprehensive approach, sustainable development provides a framework for tackling the complex relationships that exist between economic growth, environmental friendliness, and human well-being.[3] Making the transition to renewable energy sources is one of the most crucial things one can do for sustainable development.[4] Finding cleaner and more sustainable ways to power our planet is becoming increasingly crucial as the present world deals with the challenges of climate change and the depletion of fossil resources.[5,6] One can lessen our environmental effects and build a more sustainable future for everybody if the shift is made.[7] The global community is currently exploring methods to mitigate its environmental impact, but refrigeration is frequently disregarded.[8] Traditional cooling methods are dependent on refrigerants that lead to climate change; however, there is a promising alternative on the horizon: magnetic refrigeration.[9,10] Using magnetic materials to cool, this innovative technology eliminates the necessity for harmful refrigerants.[11,12] By implementing magnetic refrigeration, one can establish a cooling system that is more environmentally benign and sustainable, thereby benefiting both humans and the environment.[13,14]

Amorphous metallic alloys, which are also referred to as metallic glasses, are a category of materials that are distinguished by the absence of long-range order in the atomic structure.[15,16] These alloys are typically made up of two or more metals, such as iron, cobalt, and nickel, that are rapidly cooled from a molten state at a rate that prevents crystallization. A glass-like structure with distinctive properties is produced by this rapid quenching process.[17] The magnetic characteristics of amorphous alloys significantly contrast with those of crystalline materials.[18] Amorphous magnetic alloys demonstrate improved permeability, lowered coercivity, and elevated electrical resistivity.[19,20] The unusual features stem from the absence of long-range order in the atomic structure of amorphous alloys, resulting in distinctive magnetic behaviour.[21] The distinctive characteristics of amorphous alloys have resulted in

[a] *School of Advanced Sciences, Vellore Institute of Technology, Vellore 632014, Tamil Nadu, India*
[b] *Centre For Material Science, Karpagam Academy of Higher Education, Coimbatore - 641021, India*
[c] *Department of Physics, Karpagam Academy of Higher Education, Coimbatore - 641021, India*
[d] *Defence Metallurgical Research Laboratory, Hyderabad 500058, Telangana, India*
[e] *School of Physics, University of Hyderabad, Hyderabad 500046, India*
[f] *Ceramic Composites Laboratory, Centre for Functional Materials, Vellore Institute of Technology, Vellore, 632014, Tamil Nadu, India. E-mail: madhuriw12hotmail@gmail.com*

their extensive utilisation across several technological applications.[16,22] This encompasses the advancement of high-efficiency transformers, power electronics, high-performance gadgets, sophisticated telecommunication equipment, and sensors. Moreover, amorphous alloys have been investigated for their possible application in magnetic refrigeration, a technique that provides a more sustainable and efficient alternative to conventional cooling methods.[23,24]

The operation of magnetic refrigeration systems is based on a fundamental phenomenon known as the magnetocaloric effect (MCE).[25–27] A material's reversible temperature change in response to a fluctuating magnetic field is what defines this effect.[28,29] Several thermodynamic metrics, such as the relative cooling power (RCP), the adiabatic temperature change ($\Delta T_{ad}$), and the isothermal entropy change ($-\Delta S_M$), can be used to quantify the MCE.[30] These variables are crucial indicators for assessing a material's magnetocaloric characteristics and maximizing its performance in magnetic refrigeration applications. A viable substitute for conventional vapor-compression refrigeration methods has been made possible by the development of magnetic refrigeration.[31] Environmental issues can be reduced by using magnetic refrigeration systems that use the magnetocaloric effect instead of refrigerants.[32] It's interesting to note that, in comparison to crystalline materials, a few amorphous magnetic metal alloys have been exhibiting a stronger magnetocaloric effect close to their ordering temperature.[33]

Large thermal and magnetic hysteresis are two major disadvantages of traditional materials used for magnetic refrigeration. As a result, researchers are currently investigating various materials, such as amorphous alloys, which exhibit a second-order magnetic transition.[34] The Fe–Zr–B–Cu alloy has been recognised as a viable material for magnetic refrigeration applications owing to its adjustable $T_C$ close to ambient temperature.[21,35,36] An extensive examination of this alloy's characteristics demonstrates a significant MCE, elevated electrical resistivity, and reduced hysteresis loss, rendering it a compelling option for effective heat transmission and little energy loss.[37] These alloys are perfect for magnetic refrigeration because of their exceptional magnetic entropy fluctuation and stability across a broad temperature range.[38] Through the examination of this transition, researchers can clarify the spatial dimensionality, interaction range, and symmetry of the order parameters inside the system. Moreover, the pivotal phase transition zone demonstrates power-law behaviour, indicating the system's scaling characteristics.

The structural, thermal, magnetic, and magnetocaloric characteristics of hafnium-substituted Fe–Zr–B–Cu ribbons are thoroughly investigated in the present study. The choice of this alloy system was motivated by the need to enhance the thermal stability and magnetic performance of Fe-based amorphous and nanocrystalline ribbons, which are promising candidates for environmentally friendly magnetic refrigeration technologies. The introduction of Hf is expected to influence the glass-forming ability, refine the microstructure, and tune the magnetic interactions, thereby improving the magnetocaloric response. To analyse the behaviour of these materials close to the magnetic phase transition, intensive scaling investigations were carried out utilising the Arrott plot, Kouvel–Fisher plot, and critical isotherms. The results confirm the second-order nature of the phase transition and yield reliable critical exponents consistent with universal class behaviour, while also revealing that Hf substitution enhances both the magnetic ordering and the magnetocaloric effect. These findings demonstrate the potential of Hf-modified Fe–Zr–B–Cu ribbons as efficient candidates for solid-state cooling applications.

# 2. Methods

## 2.1 Sample preparation

$Fe_{88-x}Hf_xZr_7B_4Cu_1$ ($x$ = 2 & 4) metallic glass alloys were synthesized using the vacuum arc melting (Buhler MAM1) technique. High-purity constituent elements (>99.9%) were fused in a water-cooled copper crucible in an argon environment. The ingots were inverted and re-melted four times to enhance uniformity. Rapid solidification was subsequently accomplished utilizing single roller melt-spinning apparatus functioning in a pure argon atmosphere. The melt-spinning process was optimized with the following parameters: a wheel surface velocity of 50 m $s^{-1}$, an ejection overpressure of $10^{-3}$ bar, and a nozzle-wheel with a defined separation of 2.5 mm. This optimization led to the production of ductile ribbons with thicknesses of 0.030–0.040 mm and widths of 2–3 mm.

## 2.2 Characterization techniques

A Pan-analytical X-ray powder diffractometer with a Cu Kα source ($\lambda$ = 1.5406 Å) was employed to conduct X-ray diffraction (XRD) characterization on all samples to verify phase purity. In order to determine the presence of any crystalline phases, the diffraction patterns were obtained within a suitable $2\theta$ range of 20°–80°. The amorphous character and glass-forming ability (GFA) of the samples under investigation were evaluated using differential scanning calorimetry (DSC) on a TA Instruments, Discovery SDT 650 device. In a temperature range of 573–1573 K, DSC readings were conducted in an argon atmosphere at a constant heating rate of 20 K $min^{-1}$. The magnetic field dependence of magnetization ($M$–$H$ curves) was examined using a KLA MicroSense EZ11 vibrating sample magnetometer (VSM). Measurements were conducted under isothermal conditions from 277 to 333 K using magnetic fields of up to 2.5 T.

# 3. Results and discussion

## 3.1 X-ray diffraction

The structural properties of the $Fe_{88-x}Hf_xZr_7B_4Cu_1$ ($x$ = 2 & 4) ribbons are revealed by the X-ray diffraction (XRD) pattern shown in Fig. 1(a). The pattern is notable for having large, low-intensity diffraction peaks in the 40°–50° $2\theta$ region, which is characteristic of amorphous materials. According to earlier research,[39,40] a noticeable diffraction peak is seen at $2\theta$ = 45°, which is the typical peak of Fe-based alloys. The existence of this peak suggests a partially crystalline component, which is

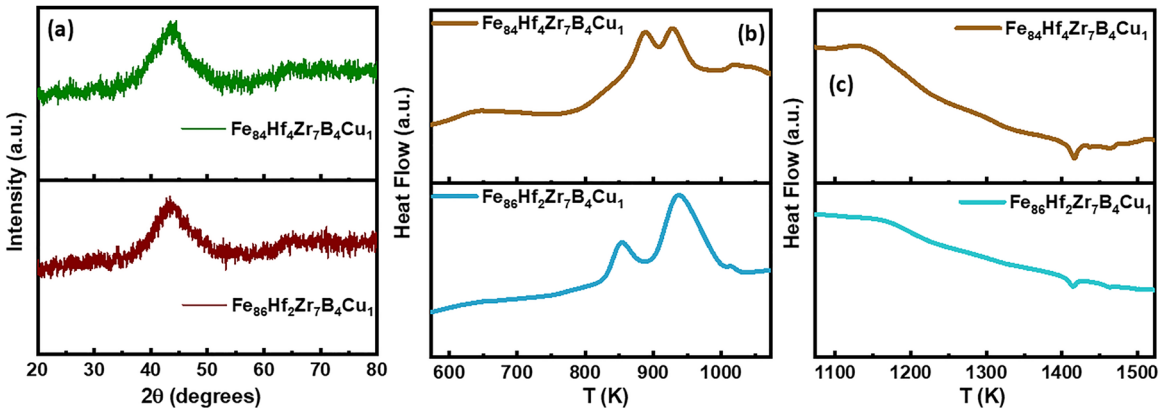


Fig. 1 (a) XRD of $Fe_{86}Hf_2Zr_7B_4Cu_1$ and $Fe_{84}Hf_4Zr_7B_4Cu_1$ ribbons and (b) and (c) DSC of $Fe_{86}Hf_2Zr_7B_4Cu_1$ and $Fe_{84}Hf_4Zr_7B_4Cu_1$ ribbons.

probably due to the intrinsic characteristics of the alloy.[41] Nonetheless, it appears from the prominent broad peaks that the $Fe_{88-x}Hf_xZr_7B_4Cu_1$ ($x$ = 2 & 4) ribbons are mostly amorphous. The synthesis procedure effectively produced an amorphous Fe-based alloy with few crystalline phases, which is essential for maximizing its mechanical and magnetic properties, according to the combined XRD data.

### 3.2 Differential scanning analysis

The thermal characteristics of the $Fe_{88-x}Hf_xZr_7B_4Cu_1$ ($x$ = 2 & 4) ribbons have been examined by differential scanning calorimetry (DSC). The curves illustrated in Fig. 1(b) and (c) convey essential data on the liquidus temperature ($T_l$) and the initial crystallisation temperature ($T_x$).[42] The GFA parameter $\alpha$ is calculated using eqn (1).

$$\alpha = \frac{T_x}{T_l} \tag{1}$$

The thermodynamic parameter $P_{HSS}$, recently introduced as a criterion for evaluating the glass-forming ability (GFA) of metallic glasses, was computed for $Fe_{88-x}Hf_xZr_7B_4Cu_1$ ($x$ = 2 & 4) ribbons using eqn (2).

$$P_{HSS} = \Delta H^{Chem}\left(\frac{\Delta S_C}{R}\right)\left(\frac{\Delta S_\sigma}{k_B}\right) \tag{2}$$

where $\Delta H^{Chem}$ represents the enthalpy of chemical mixing, $\Delta S_\sigma$ indicates the mismatch entropy, $\Delta S_C$ denotes the configurational entropy, $k_B$ is the Boltzmann constant, and $R$ is the universal gas constant.[43,44] The calculated values of $\alpha$ and $P_{HSS}$ were determined and presented in Table 1. These values yield significant insights into the GFA of the $Fe_{88-x}Hf_xZr_7B_4Cu_1$ ($x$ = 2 & 4) ribbons, facilitating a thorough comprehension of the thermodynamic and kinetic processes that dictate their GFA. The systematic increase in the $\alpha$ parameter with hafnium concentration implies a heightened degree of amorphicity in the material. Furthermore, the observed decrease in $P_{HSS}$ values with increasing hafnium content (2–4 at%) in the $Fe_{88-x}Hf_xZr_7B_4Cu_1$ ($x$ = 2 & 4) ribbons suggests an enhancement of glass-forming ability, resulting in more amorphous ribbons.[45] By elucidating the correlations between these parameters and the GFA, this study contributes to the development of a more robust framework for designing and optimizing metallic glasses with tailored properties.

Table 1 Thermal properties of $Fe_{88-x}Hf_xZr_7B_4Cu_1$ ($x$ = 2 & 4) ribbons

| Compositions | $T_x$ (K) | $T_l$ (K) | $\alpha$ | $\Delta H^{chem}$ | $\frac{\Delta S_\sigma}{k_B}$ | $\frac{\Delta S_c}{R}$ | $P_{HSS}$ (kJ mol$^{-1}$) |
|---|---|---|---|---|---|---|---|
| $Fe_{86}Hf_2Zr_7B_4Cu_1$ | 840.76 | 1592.61 | 0.53 | −13.01 | 0.10 | 0.568 | −0.755 |
| $Fe_{84}Hf_4Zr_7B_4Cu_1$ | 876.88 | 1580.30 | 0.55 | −14.02 | 0.09 | 0.636 | −0.883 |

### 3.3 Magnetic properties

Fig. 2(a) and (b) present the temperature-dependent magnetisation curves for the $Fe_{88-x}Hf_xZr_7B_4Cu_1$ ($x$ = 2 & 4) ribbons, measured at an applied magnetic field of 100 Oe. Notably, the $M$–$T$ curve exhibits a single, sharp magnetic transition from paramagnetic (PM) to ferromagnetic (FM) behaviour upon cooling. This transition is characterized by a distinct drop in magnetization, indicating the onset of paramagnetic ordering. To determine the Curie transition temperature ($T_C$), we analyzed the derivative $\frac{dM}{dT}$ curves (inset, Fig. 2(a) and (b)), identifying the critical point at $T_C$ = 298 K and 312 K for the $Fe_{86}Hf_2Zr_7B_4Cu_1$ and $Fe_{84}Hf_4Zr_7B_4Cu_1$ ribbons, respectively.

The magnetic susceptibility of the paramagnetic phase follows the Curie–Weiss law, demonstrating a temperature-dependent relationship expressed as

$$\chi(T) = \frac{C}{(T-\theta)} \tag{3}$$

where $C$ is the Curie constant and $\theta$ is the Curie–Weiss temperature. The right side of Fig. 2(a) and (b) demonstrates that the inverse magnetic susceptibility ($1/\chi$) against the temperature curve is precisely matched by the Curie–Weiss model, thereby validating this law. A fit to the experimental data yields $C$ = 0.127 emu K mol$^{-1}$, $\theta$ = 300.7 K and an effective magnetic moment ($\mu_{eff}$) of 1.01$\mu_B$ for the $Fe_{86}Hf_2Zr_7B_4Cu_1$ ribbons and $C$ = 0.124 emu K mol$^{-1}$, $\theta$ = 316.6 K and an effective magnetic moment ($\mu_{eff}$) of 0.96$\mu_B$ for the $Fe_{84}Hf_4Zr_7B_4Cu_1$ ribbons.

The FM–PM phase transition of the $Fe_{88-x}Hf_xZr_7B_4Cu_1$ ($x$ = 2 & 4) ribbons was examined in relation to the magnetic field dependency of the initial magnetization, $M(H)$. Fig. 3(a) and

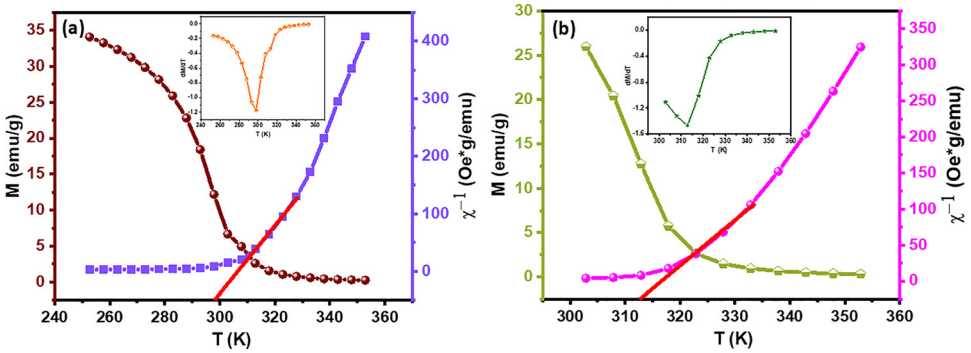


Fig. 2 $M$–$T$ and magnetic susceptibility, where the inset image is the derivative of the $M$–$T$ of the (a) $Fe_{86}Hf_2Zr_7B_4Cu_1$ and (b) $Fe_{84}Hf_4Zr_7B_4Cu_1$ ribbons.

4(a) depict the $M$–$H$ curves recorded at temperatures between 277 K and 333 K, under magnetic fields of 0–2.5 T. The curves demonstrate a pronounced rise in magnetization at low fields, subsequently reaching saturation at high fields, which aligns with ferromagnetic characteristics. The $M$–$H$ response is ascribed to the material's magnetic ordering and spin alignment.[46]

### 3.4 Scaling analysis

A comprehensive analysis of the critical region surrounding the Curie transition temperature ($T_C$) is necessary to clarify the nature of the ferromagnetic (FM) to paramagnetic (PM) phase transition.[47] The critical behavior in this region must be investigated in order to gain a comprehensive understanding of the magnetic phase transition. Nevertheless, the analysis of critical phenomena in the vicinity of $T_C$ presents a challenge, as the transition can be substantially influenced by the applied magnetic field, which could potentially induce a discontinuity in the order parameter.[48] The distinction between first-order and second-order transitions can be complicated by the field-induced effect, which can obscure the intrinsic characteristics of the phase transition. Consequently, it is imperative to meticulously evaluate the magnetic field's influence on the transition in order to precisely ascertain the FM–PM phase transition's nature.[49]

The scaling hypothesis is utilized to investigate the magnetic phase transition by using Arrott plots and critical exponents in order to clarify the critical behaviour of our samples near the $T_C$.[12,50] In particular, critical exponents $\beta$, $\gamma$, and $\delta$ were extracted, which offers a deeper understanding of the underlying physics. The ordering of the magnetic moments is characterized by the exponent $\beta$, which is associated with spontaneous magnetization ($M_S$) just below $T_C$. The divergence of magnetic susceptibility is denoted by the exponent $\gamma$, which is associated with the critical magnetization isotherm at $T_C$. In the meantime, the magnetic response in the paramagnetic regime is shown by the exponent $\delta$, which is associated with the initial magnetic susceptibility just above $T_C$. The intrinsic

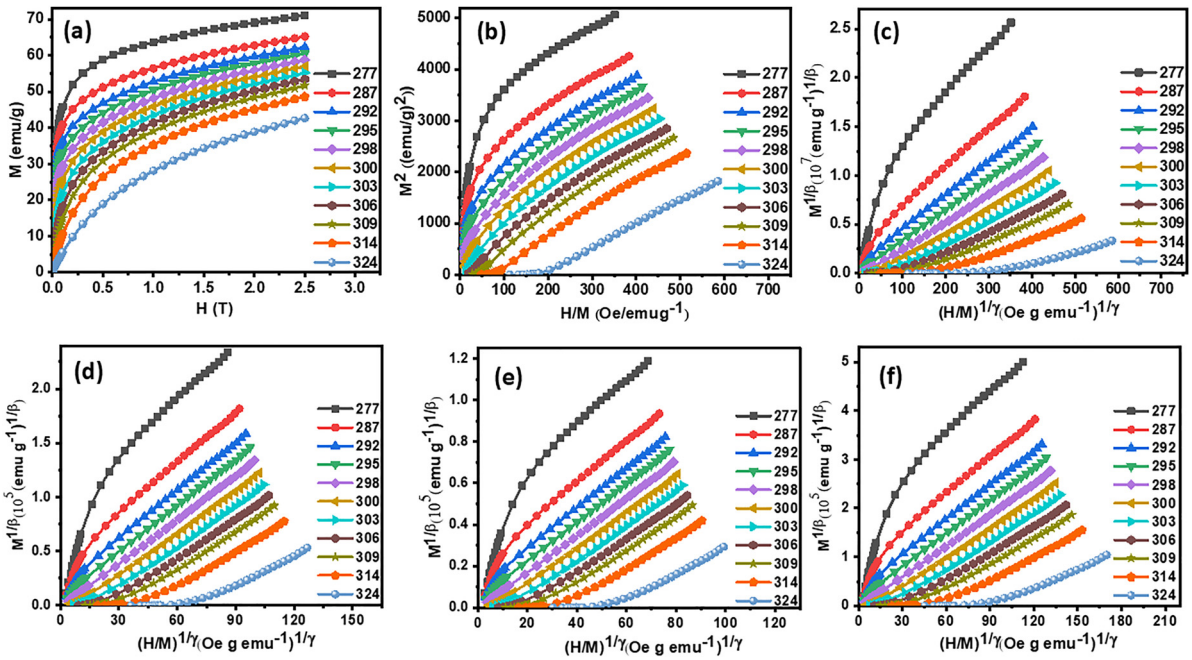


Fig. 3 (a) Isothermal curve, (b) Arrott plot, and MAPs of the (c) tricritical mean-field model, (d) 3D Heisenberg model, (e) 3D-Ising model and (f) 3-XY model of the $Fe_{86}Hf_2Zr_7B_4Cu_1$ ribbons.

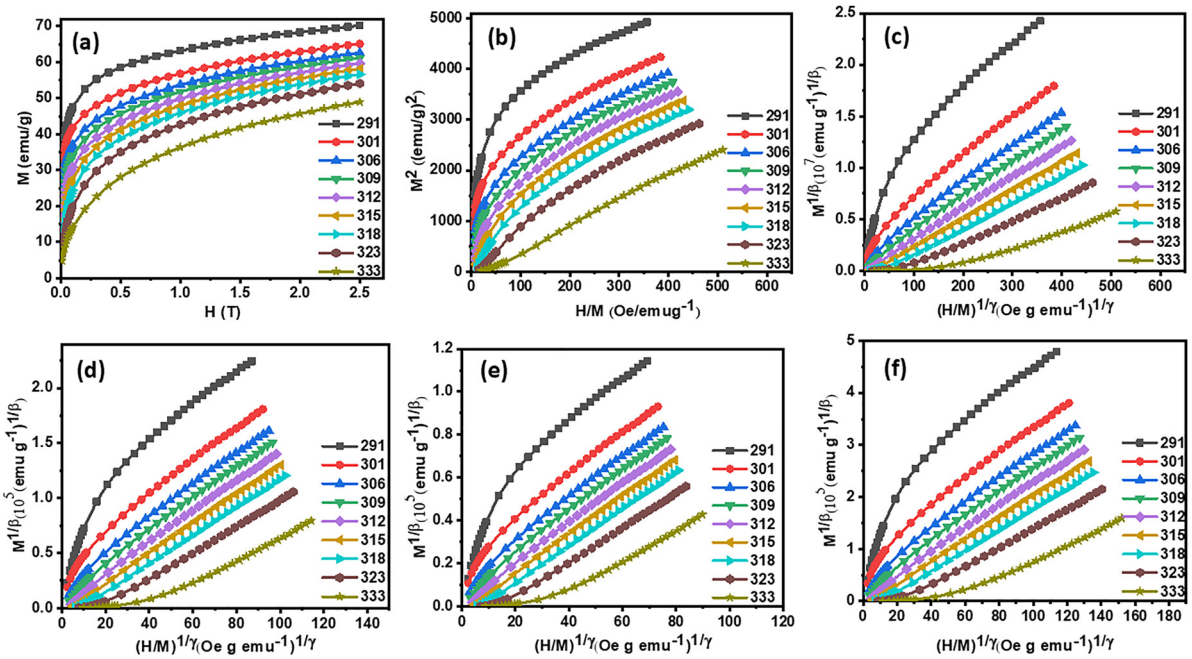


Fig. 4 (a) Isothermal curve, (b) Arrott plot, and MAPs of the (c) tricritical mean-field model, (d) 3D Heisenberg model, (e) 3D-Ising model and (f) 3-XY model of the $Fe_{84}Hf_4Zr_7B_4Cu_1$ ribbons.

character of the ferromagnetic–paramagnetic phase transition is revealed by examining these critical exponents, thereby supplying valuable information regarding the underlying magnetic interactions and fluctuations.[51]

Five theoretical models can effectively describe magnetic interactions in materials, each of which is distinguished by unique critical exponents. The mean-field model ($\beta$ = 0.5, $\gamma$ = 1.0, $\delta$ = 3.0), tri-critical mean-field model ($\beta$ = 0.25, $\gamma$ = 1.0, $\delta$ = 5.0), three-dimensional (3D) Heisenberg model ($\beta$ = 0.365, $\gamma$ = 1.336, $\delta$ = 4.8), three-dimensional (3D)-Ising model ($\beta$ = 0.325, $\gamma$ = 1.24, $\delta$ = 4.82) and 3-XY ($\beta$ = 0.345 and $\gamma$ = 1.316, $\delta$ = 4.81) are among the models.[52] A basic framework for comprehending the relationship between magnetic field, magnetization, and temperature is the equation of state, which was utilized to examine the magnetic behaviour of the system. To establish which theoretical model best described the magnetic interactions in our material and so provide insight into its underlying magnetic properties, the critical exponents that were determined empirically from the above models were compared.

$$\left(\frac{H}{M}\right)^{\frac{1}{\gamma}} = a\left(\frac{T-T_C}{T}\right) + b(M)^{\frac{2}{\beta}} \quad (4)$$

Eqn (5)–(7) of the exponent derived from $M$ measurements are presented below:

$$M_s(T) = m_0(-\varepsilon)^{\beta}; \quad T < T_C, \quad \varepsilon < 0 \quad (5)$$

$$\chi_0^{-1}(T) = \left(\frac{h_0}{m_0}\right)(\varepsilon)^{\gamma}; \quad T > T_C, \quad \varepsilon > 0 \quad (6)$$

$$M(H) = DB^{\frac{1}{\delta}}; \quad T = T_C, \quad \varepsilon = 0 \quad (7)$$

where $\varepsilon = \frac{(T-T_C)}{T_C}$ indicates the reduced temperature, $\chi_0^{-1}$ is the inverse zero-field susceptibility, $D$ is the critical amplitude, $B$ is the applied magnetic field, $M_s$ marks the spontaneous magnetization, and $h_0$ and $m_0$ are the critical amplitude.[51]

### 3.5 Critical analysis

Furthermore, the magnetic phase transition order and the properties of these materials at the $T_C$ are examined using Landau theory. The theoretical framework suggests that the sequence of magnetic phase changes can be deduced from the interaction between electron and magnetoelastic coupling. For a second-order phase transition near $T_C$, the Gibbs free energy ($G$) can be articulated as a Taylor series expansion in relation to $M$

$$G(M,T) = G_0 + \frac{1}{2}A(T)M^2 + \frac{1}{4}B(T)M^4 + \frac{1}{6}C(T)M^6 + \ldots - HM, \quad (8)$$

where the Landau coefficients $A$, $B$, and $C$, denote the electron condensation energy, elastic coupling, and magnetoelastic coupling, respectively. By simplifying eqn (8) by partial differentiation and disregarding higher-order terms, the equation can be reduced to eqn (9).

$$\frac{\partial G(M,T)}{\partial M} = A(T)M + B(T)M^3 + \ldots - H \quad (9)$$

At equilibrium, where the Gibbs free energy reaches its minimum, eqn (9) simplifies to:

$$\frac{H}{M} = A(T) + B(T)M^2 \quad (10)$$

This expression delineates a basic relationship among the magnetic field, magnetization, and temperature, yielding

significant insights into the magnetic phase transition and the material's behavior near $T_C$.[53]

The characteristics of the phase transition were analyzed using eqn (10) and the Arrott plots ($M^2$ against $\frac{H}{M}$ curves) at various temperatures are plotted as depicted in Fig. 3(b) and 4(b). The consistently positive slopes in these plots fulfill the Banerjee criterion, clearly signifying a second-order magnetic phase transition. This conclusion is substantiated by the lack of negative slopes, which are characteristic of first-order transitions. The positive slopes indicate a continuous, reversible transition, consistent with the predictions of mean-field theory.[54]

Using experimental magnetization ($M$) data acquired for the compounds under study, the modified Arrott plot (MAP) analysis is used to clarify the nature of the magnetic phase transition around the Curie transition temperature ($T_C$). Eqn (11) is used to build the MAP curves, which offered important information about the phase transition properties and underlying magnetic interactions.[51]

$$\left(\frac{\mu_0 H}{M}\right)^{\frac{1}{\gamma}} = a\left(\frac{T - T_c}{T}\right) + bM^{\frac{1}{\beta}} \tag{11}$$

where $a$ and $b$ are constants.

The MAP isotherms of $M^{\frac{1}{\beta}}$ *versus* $\left(\frac{H}{M}\right)^{\frac{1}{\gamma}}$ were constructed for $Fe_{88-x}Hf_xZr_7B_4Cu_1$ ($x$ = 2 & 4) ribbons utilizing four critical exponent models: the tricritical mean-field, 3D-Heisenberg, 3-XY and 3D-Ising models (Fig. 3(c)–(f) and 4(c)–(f)). This study assesses the material's critical behaviour, elucidating its magnetic properties.

The identification of the optimal model for critical exponent determination is complicated by the quasi-straight and nearly parallel lines. This phenomenon underscores the inherent challenges of accurately identifying critical behaviour, as the convergent linear trends obscure the distinctions between models.

To accurately ascertain the optimal model for the experimental data, relative slope (RS) analysis was utilized, a precise metric for assessing model fidelity at the critical juncture. The RS is characterized by

$$\mathrm{RS} = \frac{S(T)}{S(T_C)} \tag{12}$$

offering a quantitative assessment of the slope variation between neighbouring isotherms. Through the computation of the RS for each model, the model with the RS value closest to one is the most suitable model for precisely characterizing the optimal model of critical analysis.[55] Given this criterion, the 3D-Heisenberg model is the most appropriate for all the samples, as illustrated in Fig. 5(a) and (b). And the experimental values are most closely aligned with the theoretical predictions of the 3D Heisenberg model, as evidenced by the deviation analysis of the critical exponents, which is shown in Table S2. This implies that the magnetic interactions in the alloys under investigation are primarily short-range and isotropic in nature, which is a defining feature of the Heisenberg universality class.

The spontaneous magnetization ($M_S(T)$) and inverse susceptibility ($\chi_0^{-1}(T)$) are calculated by linear extrapolation in the high-field regime to the intercepts with the axes $M^{\frac{1}{\beta}}$ and $\left(\frac{H}{M}\right)^{\frac{1}{\gamma}}$, respectively. Fig. 6(a) and (b) illustrates the $M_S(T)$ and $\chi_0^{-1}(T)$ that resulted. The critical exponents $\beta$, $\gamma$, and $T_C$ were revised as a result of the subsequent fitting of the $M_S(T)$ and $\chi_0^{-1}(T)$ data to eqn (5) and (6), respectively. These revised values are summarised in Table 3.

The Kouvel–Fisher (KF) method was implemented to enhance the critical exponents and optimise comparisons with prior calculations. This method employs an alternative analytical expression of the power law, which facilitates a more precise determination of the critical exponents. In particular, the KF method entails the plotting of $\left[\frac{M_S}{\frac{dM_S}{dT}}\right]$ *versus* $T$ and $\left[\frac{\chi_0^{-1}}{\frac{d\chi_0^{-1}}{dT}}\right]$ *versus* $T$ as shown in Fig. 6(c) and (d), resulting in straight lines with inclinations of $\frac{1}{\beta}$ and $\frac{1}{\gamma}$, respectively. The $T_C$

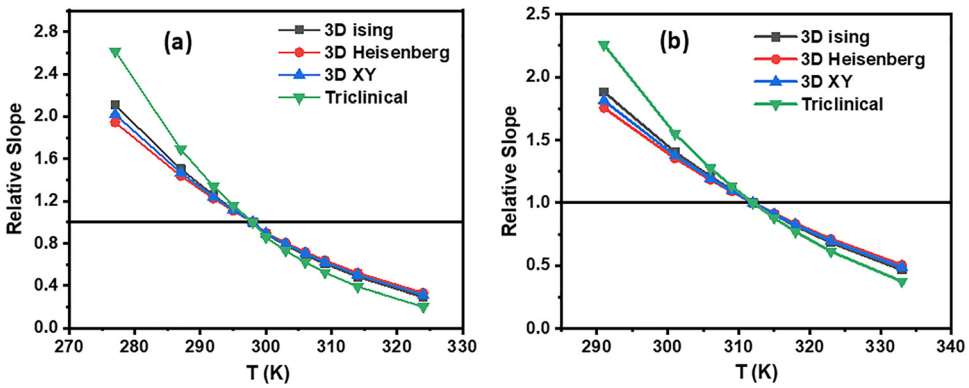


Fig. 5 Relative slope *versus* temperature curve of (a) $Fe_{86}Hf_2Zr_7B_4Cu_1$ and (b) $Fe_{84}Hf_4Zr_7B_4Cu_1$ ribbons.

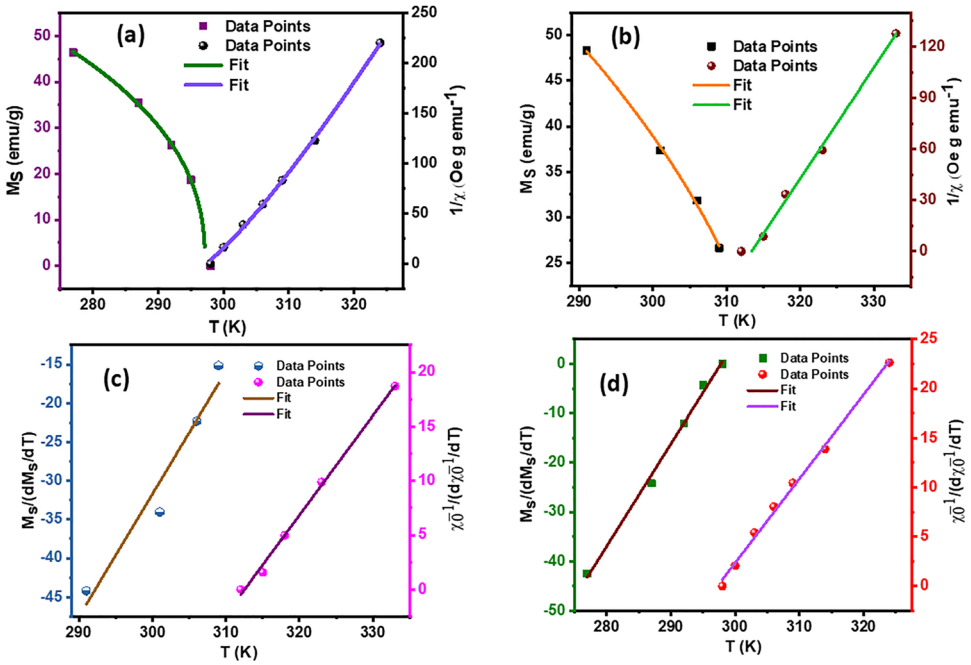


Fig. 6 Spontaneous magnetisation and inverse initial susceptibility with the fitting curves of the (a) $Fe_{86}Hf_2Zr_7B_4Cu_1$ and (b) $Fe_{84}Hf_4Zr_7B_4Cu_1$ ribbons, and KF plots of the (c) $Fe_{86}Hf_2Zr_7B_4Cu_1$ and (d) $Fe_{84}Hf_4Zr_7B_4Cu_1$ ribbons.

Table 2 Magnetocaloric properties of the $Fe_{88-x}Hf_xZr_7B_4Cu_1$ ($x$ = 2 & 4) ribbons

| Compositions | $T_C$ (K) | $-\Delta S_M$ (J kg$^{-1}$ K$^{-1}$) | $\Delta T_{FWHM}$ (K) | RCP (J kg$^{-1}$) |
|---|---|---|---|---|
| $Fe_{86}Hf_2Zr_7B_4Cu_1$ | 298 | 1.94 | 31.44 | 61.23 |
| $Fe_{84}Hf_4Zr_7B_4Cu_1$ | 312 | 1.65 | 19.95 | 33.00 |

is represented by the intercepts on the $X$-axis. Critical exponents that are consistent with previous calculations were determined from the fitted straight lines in the KF plots.[56]

In addition, the third critical exponent $\delta$ is directly determined from the critical isotherm $M(T_C,H)$. Fig. S1(a) and (b) illustrates the magnetic field dependence of magnetization at $T = T_C$ for the samples. The figure illustrates the same plot on a log–log scale. The log($M$) *versus* log($H$) graph, as per eqn (7), produces a straight line with a slope of $\frac{1}{\delta}$. Correspondingly, $\delta$ = 4.70 for $Fe_{86}Hf_2Zr_7B_4Cu_1$ ribbons and 4.54 for $Fe_{84}Hf_4Zr_7B_4Cu_1$ ribbons, respectively.

The Widom scaling relation,[57] which is defined as $\delta = 1 + \frac{\gamma}{\beta}$, connects the critical exponents obtained from the static scaling analysis. This relation and the previously estimated values of $\gamma$ and $\beta$ obtained through the mean-field method were used to calculate $\delta$ as shown in Table 3. The results were found to be in close agreement with the values extracted from the critical isotherms. The consistency of the analysis is validated by the Widom scaling relation, which also reinforces the reliability of the critical exponents that were determined using the mean-field method.

Table 3 Comparison of critical exponents for the $Fe_{88-x}Hf_xZr_7B_4Cu_1$ ($x$ = 2 & 4) ribbons from various theoretical models

| Composition | Technique | $\beta$ | $\gamma$ | $\delta$ | Ref. |
|---|---|---|---|---|---|
| $Fe_{86}Hf_2Zr_7B_4Cu_1$ | Modified Arrott | 0.410 | 1.196 | — | Present work |
| | Kouvel–Fisher | 0.481 | 1.172 | — | Present work |
| | CIA | — | — | 3.92 | Present work |
| | Widom scaling | — | — | 4.70 | Present work |
| $Fe_{84}Hf_4Zr_7B_4Cu_1$ | MAP | 0.517 | 1.002 | — | Present work |
| | KF | 0.632 | 1.091 | — | Present work |
| | CIA | — | — | 2.93 | Present work |
| | WSR | — | — | 4.54 | Present work |
| 3D Heisenberg | Theory | 0.365 | 1.336 | 4.80 | 52 |
| 3D Ising | Theory | 0.325 | 1.24 | 4.82 | 45 |
| 3 XY | Theory | 0.345 | 1.316 | 4.81 | 45 |
| Triclinical mean field | Theory | 0.25 | 1 | 5 | 52 |

### 3.6 Magnetocaloric effect

A system's total entropy ($S$) is determined by eqn (13).

$$S = S_{magnetic} + S_{lattice} + S_{electronic} \quad (13)$$

which combines isothermal magnetic entropy ($S_{magnetic}$), lattice entropy ($S_{lattice}$), and electronic entropy ($S_{electronic}$).[58] This approximation allows for the estimation of $\Delta S$ based on the magnetization isotherms $M$ ($H$, $T$) depicted in Fig. 7(a) and (b). The isothermal field-induced magnetic entropy change ($\Delta S_M$) from 0 to $H_{max}$ can be calculated using the following relation, according to thermodynamic theory:

$$\Delta S(T,H) = S_M(T,H) - S_M(T,0) = \int_0^H \left(\frac{\partial s}{\partial H}\right)_T dH \quad (14)$$

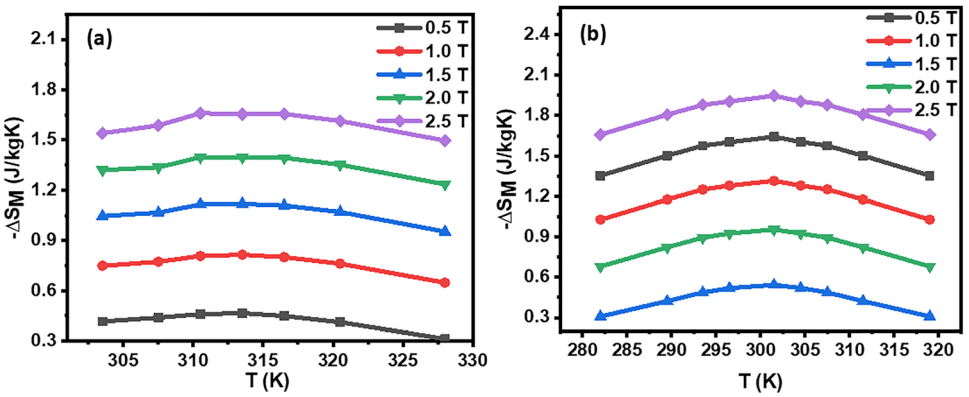


Fig. 7 Magnetic entropy *versus* temperature graph of (a) $Fe_{86}Hf_2Zr_7B_4Cu_1$ and (b) $Fe_{84}Hf_4Zr_7B_4Cu_1$ ribbons.

Eqn (15) is derived from the Maxwell relation

$$\left(\frac{\partial s}{\partial H}\right)_T = \left(\frac{\partial M}{\partial T}\right)_H \quad (15)$$

which establishes a fundamental connection between magnetization and entropy. The isothermal magnetic entropy change can be precisely determined by integrating the magnetization isotherms, which offers valuable insights into the thermodynamic properties of the material, which is given as[58]

$$\Delta S_M(T,H) = \int_0^H \left(\frac{\partial M}{\partial T}\right)_H \mathrm{d}H \quad (16)$$

The magnetic entropy change that was obtained has been depicted as a function of temperature in Fig. 7(a) and (b). Around the Curie transition temperature ($T_C$), the magnetic entropy change ($|\Delta S_M|$) displays a crest, and its amplitude increases steadily as the magnetic field intensity is increased. This behaviour is a sign of the material's suitability for magnetocaloric applications.[59] It is remarkable that the material is capable of achieving a maximal $|\Delta S_M|$ value of 1.94 J kg$^{-1}$ K$^{-1}$ for the $Fe_{86}Hf_2Zr_7B_4Cu_1$ ribbons and 1.65 J kg$^{-1}$ K$^{-1}$ for the $Fe_{84}Hf_4Zr_7B_4Cu_1$ ribbons, respectively, under a 2.5 T magnetic field, which underlines its potential for efficient thermal energy conversion. The material's responsiveness to magnetic field fluctuations is emphasized by the dramatic entropy change at $T_C$, rendering it an appealing candidate for next-generation magnetic refrigeration technologies.

Besides magnetic entropy change, a vital metric for evaluating the cooling efficacy of a refrigerant is the relative cooling power (RCP).[60] RCP offers a thorough assessment of a material's capacity for heat transfer in an optimal refrigeration cycle, considering both the extent of the maximum magnetic entropy change and its full width at half maximum ($\Delta T_{FWHM}$).[61] By taking these elements into account, RCP provides a more refined assessment of a material's refrigeration properties. The RCP values for the examined material in a 2.5 T magnetic field are presented in Table 2. These findings offer significant insights into the material's capacity for effective heat transfer and its appropriateness for diverse magnetocaloric applications. A comparison between the magnetocaloric characteristics of the present work and those of other Fe-based alloys is summarized in Table S1. The results unequivocally show that our alloy performs noticeably better than the previously documented Fe-based systems, as evidenced by greater values of magnetic entropy change ($\Delta S_M$), Curie transition temperature ($T_C$) near to room temperature, and relative cooling power (RCP), all of which are critical for practical magnetic refrigeration applications.

## 4. Conclusion

This study presents a thorough examination of $Fe_{88-x}Hf_xZr_7B_4Cu_1$ ($x$ = 2 & 4) ribbons and aims to clarify the structural, magnetic, magnetocaloric, and critical analysis. The $Fe_{88-x}Hf_xZr_7B_4Cu_1$ ($x$ = 2 & 4) ribbons had an amorphous structure. The magnetic phase transition temperature (MPT) for the compounds was 298 K and 312 K for the $Fe_{86}Hf_2Zr_7B_4Cu_1$ and $Fe_{84}Hf_4Zr_7B_4Cu_1$ ribbons, respectively. Furthermore, our investigation focused on the spontaneous magnetization and critical behaviour of the $Fe_{88-x}Hf_xZr_7B_4Cu_1$ ($x$ = 2 & 4) ribbons, employing a variety of research methodologies, including modified Arrott plots, the Kouvel–Fisher methodology, and critical isotherm analysis. Our investigation yielded consistent critical exponents ($T_C$, $\beta$, $\gamma$, and $\delta$) that were in remarkable agreement with the theoretical predictions of the mean-field model. The experimental findings are primarily influenced by short-range interactions near the Curie transition temperature ($T_C$), as indicated by these models. This provides valuable insights into the fundamental principles that govern the critical behavior of these intricate materials. Our research reveals that the $Fe_{88-x}Hf_xZr_7B_4Cu_1$ ($x$ = 2 & 4) ribbons have great potential for magnetocaloric applications. For instance, the $Fe_{86}Hf_2Zr_7B_4Cu_1$ ribbons can provide a relative cooling power of approximately 61.23 J kg$^{-1}$ at a temperature of 298 K, while the $Fe_{84}Hf_4Zr_7B_4Cu_1$ ribbons have a relative cooling power of 33.0 J kg$^{-1}$ at 312 K under a 2.5 T magnetic field.

## Conflicts of interest

There are no conflicts to declare.

## Data availability

The data supporting this article have been included as part of the supplementary information (SI). Supplementary information is available. See DOI: https://doi.org/10.1039/d5ma00922g.

## Acknowledgements

The authors acknowledge SAS, VIT University, for providing financial support and research facilities. We acknowledge DMRL, Hyderabad, for the melt spinning, and XRD and Arc melting facilities.

## References

1 M. Hajian and S. Jangchi Kashani, Evolution of the concept of sustainability. From Brundtland Report to sustainable development goals, in *Sustainable Resource Management*, Elsevier, 2021, pp. 1–24, DOI: 10.1016/B978-0-12-824342-8.00018-3.
2 E. Holden, K. Linnerud and D. Banister, The Imperatives of Sustainable Development, *Sustainable Dev.*, 2017, **25**, 213–226.
3 J. Mensah, Sustainable development: Meaning, history, principles, pillars, and implications for human action: Literature review, *Cogent Soc. Sci.*, 2019, **5**, 1653531.
4 S. Algarni, V. Tirth, T. Alqahtani, S. Alshehery and P. Kshirsagar, Contribution of renewable energy sources to the environmental impacts and economic benefits for sustainable development, *Sustain. Energy Technol. Assessments*, 2023, **56**, 103098.
5 J. Wang and W. Azam, Natural resource scarcity, fossil fuel energy consumption, and total greenhouse gas emissions in top emitting countries, *Geosci. Front.*, 2024, **15**, 101757.
6 K. K. Jaiswal, *et al.*, Renewable and sustainable clean energy development and impact on social, economic, and environmental health, *Energy Nexus*, 2022, **7**, 100118.
7 A. Pan, S. Xu, S. Anees and H. Zaidi, Environmental impact of energy imports: Natural resources income and natural gas production profitability in the Asia-Pacific Economic Cooperation Countries, *Geosci. Front.*, 2024, **15**, 101756.
8 O. Oloruntobi, *et al.*, Effective technologies and practices for reducing pollution in warehouses - A review, *Clean. Eng. Technol.*, 2023, **13**, 100622.
9 O. Chdil, M. Bikerouin, M. Balli and O. Mounkachi, New horizons in magnetic refrigeration using artificial intelligence, *Appl. Energy*, 2023, **335**, 120773.
10 M. Masche, J. Liang, K. Engelbrecht and C. R. H. Bahl, Improving magnetic cooling efficiency and pulldown by varying flow profiles, *Appl. Therm. Eng.*, 2022, **215**, 118945.
11 H. Zhang, *et al.*, Review on the materials and devices for magnetic refrigeration in the temperature range of nitrogen and hydrogen liquefaction, *Phys. B*, 2019, **558**, 65–73.
12 A. Vinod, D. A. Babu and W. Madhuri, Near room temperature magnetocaloric effect in Co: $LaFe_{13-x}$ six ribbons through melt spinning: Boosting δTFWHM and Curie temperature, *Intermetallics*, 2025, **185**, 108896.
13 U. Lucia and G. Grisolia, Magnetocaloric Refrigeration in the Context of Sustainability: A Review of Thermodynamic Bases, the State of the Art, and Future Prospects, *Energies*, 2024, **17**, 3585.
14 C. Aprea, A. Greco, A. Maiorino and C. Masselli, Magnetic refrigeration: an eco-friendly technology for the refrigeration at room temperature, *J. Phys.:Conf. Ser.*, 2015, **655**, 012026.
15 M. Chen, A brief overview of bulk metallic glasses, *NPG Asia Mater.*, 2011, **3**, 82–90.
16 Z. Feng, H. Geng, Y. Zhuang and P. Li, Progress, Applications, and Challenges of Amorphous Alloys: A Critical Review, *Inorganics*, 2024, **12**, 232.
17 B. El Ouahbi, *et al.*, Magnetic phase transition and magnetocaloric effect in amorphous $Gd_{52}Fe_{28}B_{20}$ alloy, *Appl. Phys. A: Mater. Sci. Process.*, 2024, **130**, 559.
18 F. E. Luborsky, Magnetic properties of amorphous alloys, *J. Magn. Magn. Mater.*, 1978, **7**, 143–149.
19 R. Hasegawa, Applications of amorphous magnetic alloys in electronic devices, *J. Non-Cryst. Solids*, 2001, **287**, 405–412.
20 F. Wang, *et al.*, Soft magnetic Fe-Co-based amorphous alloys with extremely high saturation magnetization exceeding 1.9 T and low coercivity of 2 A/m, *J. Alloys Compd.*, 2017, **723**, 376–384.
21 A. Vinod, *et al.*, Glass forming ability and critical exponents in Hf-Modified Fe-Zr-B-Cu amorphous alloys for near room temperature magnetocaloric application, *Sci. Rep.*, 2025, **15**, 24223.
22 F. C. Li, *et al.*, Amorphous–nanocrystalline alloys: fabrication, properties, and applications, *Mater. Today Adv.*, 2019, **4**, 100027.
23 S. Wei, H. Shen, L. Zhang, F. Cao and J. Sun, Magnetic properties and magnetocaloric effects of rare-earth based high-entropy amorphous microwires, *J. Mater. Res. Technol.*, 2024, **33**, 6216–6222.
24 A. E.-M. A. Mohamed, M. Jeong, R. S. Sheridan and M. M. Attallah, Enabling high efficiency magnetic refrigeration using laser powder bed fusion of porous $LaCe(Fe,Mn,Si)_{13}$ structures, *Addit. Manuf.*, 2022, **51**, 102620.
25 V. K. Pecharsky and K. A. Gschneidner Jr, Magnetocaloric effect and magnetic refrigeration, *J. Magn. Magn. Mater.*, 1999, **200**, 44–56.
26 M. Arejdal, A computational study of the magnetocaloric effect in the $LaCr_2Si_2C$ compound, *Polyhedron*, 2020, **183**, 114539.
27 M. Arejdal, Prediction of the magnetocaloric behaviors of the Kekulene structure for the magnetic refrigeration, *Results Phys.*, 2020, **18**, 103342.
28 S. Pajovic and S. V. Boriskina, Magnetocaloric-Effect-Enhanced Near-Field Magneto-optical Thermal Switch, *Phys. Rev. Appl.*, 2023, **20**, 014053.
29 M. Arejdal, The theoretical study of the magneto-caloric effect in a nano-structure formed on a Dendrimer structure, *Appl. Phys. A: Mater. Sci. Process.*, 2020, **126**, 829.

30 A. Vinod, D. Arvindha Babu and M. Wuppulluri, A Short Review on the Evolution of Magnetocaloric $La(Fe,Si)_{13}$ and Its Fabrication through Melt Spinning, *ACS Omega*, 2024, **9**, 11110–11128.

31 N. A. Mezaal, K. V. Osintsev and T. B. Zhirgalova, Review of magnetic refrigeration system as alternative to conventional refrigeration system, *IOP Conf. Ser. Earth Environ. Sci.*, 2017, **87**, 032024.

32 S. Mellari, Introduction to magnetic refrigeration: magnetocaloric materials, *Int. J. Air-Cond. Refrig.*, 2023, **31**, 5.

33 Q. Wang, L. L. Pan, B. Z. Tang, D. Ding and L. Xia, Outstanding magnetocaloric properties at ambient temperature of a $Fe_{88}La_4Ce_3B_5$ amorphous alloy, *J. Non-Cryst. Solids*, 2022, **580**, 121394.

34 H. Biswal, V. Singh, R. Nath and J. R. Sahu, Magnetic properties and near-room-temperature large magnetocaloric effect in $(La_{1-x}Bi_x)_{0.67}Ba_{0.33}MnO_3$ ($x$ = 0–0.3) ceramics, *Mater. Res. Bull.*, 2021, **133**, 111030.

35 W. Yang, *et al.*, Low-Temperature Magnetic Properties and Magnetocaloric Effect of Fe–Zr–Cu Amorphous Alloys, *J. Low Temp. Phys.*, 2020, **200**, 51–61.

36 A. Vinod, A. B. Diraviam, M. R. Muthuvel and M. Wuppulluri, Rare earth-free magnetocaloric material $Fe_{82}Hf_6Zr_7B_4Cu_1$ for high-temperature applications, *RSC Adv.*, 2025, **15**, 15310–15317.

37 Y. Liu, X. Fu, Q. Yu, M. Zhang and J. Liu, Significant reduction of phase-transition hysteresis for magnetocaloric $(La_1\text{-}Ce)_2Fe_{11}Si_2H$ alloys by microstructural manipulation, *Acta Mater.*, 2021, **207**, 116687.

38 L. F. Kiss, T. Kemény, V. Franco and A. Conde, Enhancement of magnetocaloric effect in B-rich FeZrBCu amorphous alloys, *J. Alloys Compd.*, 2015, **622**, 756–760.

39 C. Zhang, Z. Zhu, H. Zhang and Z. Hu, On the decolorization property of Fe–Mo–Si–B alloys with different structures, *J. Non-Cryst. Solids*, 2012, **358**, 61–64.

40 B. Lin, X. Bian, P. Wang and G. Luo, Application of Fe-based metallic glasses in wastewater treatment, *Mater. Sci. Eng. B*, 2012, **177**, 92–95.

41 T. Dai and N. Wang, Study on Magnetic Properties and Degradability of Gas Atomization Fe-Based (Fe-Si-B-P) Amorphous Powder, *J. Supercond. Nov. Magn.*, 2019, **32**, 3699–3702.

42 Z. P. Lu, H. Tan, S. C. Ng and Y. Li, The correlation between reduced glass transition temperature and glass forming ability of bulk metallic glasses, *Scr. Mater.*, 2000, **42**, 667–673.

43 B. Ramakrishna Rao, M. Srinivas, A. K. Shah, A. S. Gandhi and B. S. Murty, A new thermodynamic parameter to predict glass forming ability in iron based multi-component systems containing zirconium, *Intermetallics*, 2013, **35**, 73–81.

44 A. Vinod, A. B. Diraviam, M. R. Muthuvel and M. Wuppulluri, Exploring critical exponent and glass-forming ability of nanoperm type-$Fe_{88}Zr_7B_4Cu_1$ metallic glasses: an integrated experimental and theoretical approach, *Emergent Mater.*, 2025, 1–9.

45 A. Vinod, A. B. Diraviam, M. R. Muthuvel and M. Wuppulluri, Tailoring the GFA, -ΔSM and RC of $Fe_{86}$-$2xZr_8 + xB_5 + xCu_1$ ($x$ = 0, 1 & 2) metallic glass ribbons for magnetocaloric applications, *J. Non-Cryst. Solids*, 2025, **650**, 123376.

46 A. Murtaza, *et al.*, Magnetostructural transition, magnetocaloric effect and critical exponent analysis in $Nd(Co_{0.8}Fe_{0.2})_2$ alloy, *J. Alloys Compd.*, 2022, **895**, 162562.

47 I. Sfifir, *et al.*, Critical behavior near the paramagnetic-ferromagnetic phase transition in polycrystalline $La_{0.6}Ca_{0.2}$-$Ba_{0.15\square 0.05}MnO_3$, *Ceram. Int.*, 2016, **42**, 12956–12963.

48 M. Abassi, Z. Mohamed, J. Dhahri and E. K. Hlil, Short-range ferromagnetic order in perovskite manganite $La_{0.62}Er_{0.05}Ba_{0.33}Mn_{0.95}Fe_{0.05}O_3$, *J. Alloys Compd.*, 2016, **664**, 657–663.

49 P. Sarkar, *et al.*, Field-induced first-order to second-order magnetic phase transition in $Sm_{0.52}Sr_{0.48}MnO_3$, *Phys. Rev. B: Condens. Matter Mater. Phys.*, 2008, **78**, 012415.

50 N. Ameur, M. Triki, E. Dhahri and E. K. Hlil, Correlation between critical behavior and magnetocaloric effect for $La_{0.8-x} \times Na_{0.2-x} \times MnO_3$ ($x$ = 0 and 0.1) compounds, *Solid State Commun.*, 2019, **292**, 40–49.

51 M. Bourguiba, M. A. Gdaiem, M. Chafra and E. K. Hlil, Long-range ferromagnetic order in perovskite manganite $La_{0.67}Ba_{0.25}Ca_{0.08}$ $Mn_{(1-x)}$ Ti × $O_3$ ($x$ = 0.00, 0.05 and 0.10), *RSC Adv.*, 2020, **10**, 26326–26334.

52 C. Zhang, *et al.*, Critical behavior of intercalated quasi-van der Waals ferromagnet $Fe_{0.26}TaS_2$, *Phys. Rev. Mater.*, 2019, **3**, 0–9.

53 M. K. Rout and S. Keshri, Elastic, Magnetocaloric, and Magneto-Dielectric Properties of $Dy^{3+}$ and $La^{3+}$ Doped $Co_{0.7}Zn_{0.3}Fe_2O_4$ Ferrite Nanoparticles for Multifunctional Devices, *J. Phys. Chem. C*, 2024, **128**, 17731–17746.

54 L. Wang, M. Feizpour, P. McGuiness, D. Feizpour and Y. Zhang, Glass-forming ability, magnetic phase transition, and low-temperature magnetocaloric performance of $Ho_{60}Co_{20}Cu_{20}$ amorphous ribbon, *J. Magn. Magn. Mater.*, 2024, **610**, 172504.

55 M. S. Anwar, I. Hussain, S. N. Khan, P. Fournier and B. H. Koo, Magnetic critical behavior and room temperature magnetocaloric effect in $Ba_{1.9}Pr_{0.1}FeMoO_6$ double perovskite compound, *Mater. Res. Bull.*, 2023, **161**, 112151.

56 J. S. Kouvel and M. E. Fisher, Detailed Magnetic Behavior of Nickel Near its Curie Point, *Phys. Rev.*, 1964, **136**, A1626–A1632.

57 J. C. Debnath, P. Shamba, A. M. Strydom, J. L. Wang and S. X. Dou, Investigation of the critical behavior in $Mn_{0.94}Nb_{0.06}CoGe$ alloy by using the field dependence of magnetic entropy change, *J. Appl. Phys.*, 2013, **113**(9), 093902.

58 K. P. Shinde, *et al.*, Magnetocaloric effect and Griffiths phase analysis in a nanocrystalline $Ho_2NiMnO_6$ and $Ho_2CoMn_6$ double perovskite, *RSC Adv.*, 2023, **13**, 9099–9108.

59 A. Vinod, D. A. Babu, M. R. Muthuvel, P. Ramasamy and W. Madhuri, Critical behaviour and magnetocaloric properties of $Fe_{88}Zr_5Hf_2B_4Cu_1$ metallic glass for near-room temperature magnetic refrigeration application, *J. Mater. Chem. C*, 2025, **13**, 8228–8237.

60 A. Prusty, S. Mahana, A. Gloskovskii, D. Topwal and U. Manju, Gd induced modifications in the magnetocaloric properties of dysprosium manganites, *J. Alloys Compd.*, 2021, **883**, 160862.

61 P. Z. Z. Nehan, *et al.*, The magnetocaloric effect properties for potential applications of magnetic refrigerator technology: a review, *Phys. Chem. Chem. Phys.*, 2024, **26**, 14476–14504.